Fluid pressure response in poroelastic materials subjected to cyclic loading

Yoshitaka Kameo[a], Taiji Adachi[a, b], and Masaki Hojo[a]

a: Department of Mechanical Engineering and Science, Kyoto University
b: Computational Cell Biomechanics Team, VCAD System Research Program, RIKEN

Corresponding author:	Taiji Adachi, Ph.D.
Mailing Address:	Department of Mechanical Engineering and Science
	Kyoto University
	Yoshida-honmachi, Sakyo, Kyoto 606-8501, Japan
Telephone & Fax:	+81 (75) 753-5216
E-mail:	adachi@me.kyoto-u.ac.jp

Submitted to “Journal of the Mechanics and Physics of Solids” on December 28th, 2008
The first revision: June 2nd, 2009
The second revision: August 1st, 2009

Abstract

When cyclic loading is applied to poroelastic materials, a transient stage of interstitial fluid pressure occurs, preceding a steady state. In each stage, the fluid pressure exhibits a characteristic mechanical behavior. In this study, an analytical solution for fluid pressure in two-dimensional poroelastic materials, which is assumed to be isotropic, under cyclic axial and bending loading is presented, based on poroelasticity. The obtained analytical solution contains transient and steady-state responses. Both of these depend on three dimensionless parameters: The dimensionless stress coefficient; the dimensionless frequency; and, the axial-bending loading ratio. We focus particularly on the transient behavior of interstitial fluid pressure with changes in the dimensionless frequency and the axial-bending loading ratio. The transient properties, such as half-value period and contribution factor, depend largely on the dimensionless frequency and have peak values when its value is about 10. This suggests that, under these conditions, the transient response can significantly affect the mechanical behavior of poroelastic materials.

Keywords: Porous material, Poroelasticity, Cyclic loading, Bending moment, Transient response, Fluid pressure

1. Introduction

The presence of interstitial fluid in porous materials modifies its mechanical response due to the interaction between solid deformation and fluid flow. Two principal mechanisms are involved in this phenomenon, i.e. (i) a change in applied stress produces a change in fluid pressure and a transport of interstitial fluid (solid-to-fluid coupling), while (ii) fluid pressure and its transport cause a volume change of the matrix material (fluid-to-solid coupling). The coupling of these mechanisms leads to time-dependent mechanical behavior of the porous materials.

The coupled diffusion-deformation phenomenon in porous materials is initially investigated to understand the mechanism of soil consolidation, i.e. the progressive settlement of a soil, mainly in geomechanics. To solve the consolidation problem, Biot (1941, 1955) presented poroelasticity, which is a coupling theory for the deformation of linear elastic materials governed by Hooke's law, and interstitial fluid flow governed by Darcy's law. Poroelasticity enables us to quantify the solid-fluid coupling behavior of poroelastic materials and evaluate its time dependency. This theory has been widely applied to the mechanical analysis of biological tissues, such as bone, cartilage and cardiac muscle (Nowinski and Davis 1970; Mow *et al*., 1980; Yang and Taber, 1991), as well as that of rocks and soils (Jacob, 1940; Bredehoeft, 1967).

Poroelastic materials found in nature can be often assumed to be subjected to cyclic loading. A groundwater-saturated soil under the influence of atmospheric pressure or earth tides is the good example and its poroelastic behavior was focused on in the field of geomechanics (Jacob,

1940; Bredehoeft, 1967; Rojstaczer, 1988; Quilty and Roeloffs, 1991; Roeloffs, 1996). Many researchers in biomechanics regarded bone tissue as poroelastic material with isotropic (e.g. Harrigan and Hamilton, 1993; Weinbaum *et al*., 1994; Zhang and Cowin, 1994, Zhang *et al*., 1998) or anisotropic mechanical properties (e.g. Swan *et al*., 2003; Rémond and Naili, 2005, Rémond *et al*., 2008), and investigated the mechanical response to physiological cyclic loading. In general, after applying cyclic loading to the poroelastic materials, a transient stage of fluid pressure precedes the steady state. Despite the rapid decay of the transient stage, the materials exhibit a unique response. Particularly under the condition of intermittent loading, the transient response occurs frequently, and its contribution to the magnitude of the fluid pressure is comparably equal to that of the steady-state response. To understand poroelastic behavior in detail, it is important to investigate the transient response observed immediately after loading. However, most previous researches have been concerned only with the steady-state response; there are few reports on the transient response.

In this study, we extend the solution of poroelastic materials under cyclic uniaxial loading obtained by Kameo *et al*. (2008) by considering bending moment to investigate poroelastic behavior under more complex loading conditions. That is, we present an analytical solution of interstitial fluid pressure that includes both the transient and steady-state responses in poroelastic materials subjected to cyclic axial and bending loading. Based on the obtained solution, we demonstrate how two parameters, the loading frequency and the axial-bending loading ratio, affect the distribution, evolution, and transient properties of fluid pressure in poroelastic materials.

2. Poroelasticity

2.1 Constitutive relations

The Biot formulation of the constitutive equations for a fluid-saturated porous material is based on the assumption that both the infinitesimal deformation of porous material and the interstitial fluid flow are expressed as the linear sum of the contributions from the stress and the fluid pressure. The constitutive relations for isotropic poroelastic materials are expressed using solid strain tensor ε_{ij}, total stress tensor σ_{ij}, interstitial fluid pressure p, and variation of fluid content ζ, defined as the variation of fluid volume per unit volume of porous material:

$$\varepsilon_{ij} = \frac{1}{2G}\left(\sigma_{ij} - \frac{\nu}{1+\nu}\sigma_{kk}\delta_{ij} \right) + \frac{\alpha}{3K} p\delta_{ij} \tag{1}$$

$$\zeta = \frac{\alpha}{K}\frac{\sigma_{kk}}{3} + \frac{\alpha}{KB} p \quad , \tag{2}$$

where σ_{kk} represents a sum of the three normal stresses with the Einstein summation convention for repeated subscripts, δ_{ij} is the Kronecker delta, that is $\delta_{ij} = 1$ if $i = j$ and $\delta_{ij} = 0$ if $i \neq j$ (Detournay and Cheng, 1993; Wang, 2000; Coussy, 2004). In the above equation, G, ν and K are, respectively, the shear modulus, Poisson's ratio, and the bulk modulus under the drained condition, satisfying $K = 2G(1+\nu)/3(1-2\nu)$. The drained condition is when the fluid pressure equilibrates with the environmental pressure, usually assumed to be zero. The Biot-Willis coefficient α and Skempton coefficient B in Eqs. (1) and (2) are given by

$$\alpha = 1 - \frac{K}{K_s} \tag{3}$$

$$B = \frac{1/K - 1/K_s}{\phi/K_f + 1/K - (1+\phi)/K_s} \quad , \tag{4}$$

where K_s is the bulk modulus of the solid constituent, K_f is the bulk modulus of the fluid, and

ϕ is the porosity.

Assuming isotropic behavior of the interstitial fluid flow, which is governed by Darcy's law, the fluid flux component q_i is related to the fluid pressure gradient $p_{,i}$ as:

$$q_i = -\frac{k}{\mu} p_{,i} \quad , \tag{5}$$

where k is the permeability and μ is the dynamic viscosity of fluid. Equations (1), (2) and (5) are the constitutive equations for poroelasticity.

2.2 Governing equations

In order to study the quasi-static behavior of poroelastic materials, the linear momentum conservation equation without inertia terms, i.e. the stress equilibrium equation, is utilized in this study. The stress equilibrium equations of poroelastic materials are

$$\sigma_{ji,j} + F_i = 0 \quad , \tag{6}$$

where F_i is the component of body forces. Using the constitutive equation, Eq. (1), the equilibrium equation, Eq. (6) in the absence of body forces, and the displacement-strain relation:

$$\varepsilon_{ij} = \frac{1}{2}\left(u_{i,j} + u_{j,i}\right) \quad , \tag{7}$$

the strain compatibility equation expressed in the stress components is obtained:

$$\nabla^2 \left[\sigma_{kk} + \frac{2\alpha\left(1-2\nu\right)}{\left(1-\nu\right)} p \right] = 0 \quad , \tag{8}$$

where ∇^2 stands for the Laplace operator.

The equation of fluid continuity is expressed as:

$$\frac{\partial \zeta}{\partial t} + q_{k,k} = Q \quad , \tag{9}$$

where Q is the source density, i.e. the rate of injected fluid volume per unit volume of porous solid. Using the constitutive equation, Eq. (2), Darcy's law Eq. (5), the strain compatibility equation, Eq. (8), and Eq. (9) in the absence of fluid source, the isotropic diffusion equation for poroelasticity is eventually derived in the form:

$$c\nabla^2\left(\sigma_{kk} + \frac{3}{B}p\right) = \frac{\partial}{\partial t}\left(\sigma_{kk} + \frac{3}{B}p\right) \quad , \tag{10}$$

in which the diffusion coefficient c is given by

$$c = \frac{k}{\mu}\left[\frac{2GB^2(1-\nu)(1+\nu_u)^2}{9(1-\nu_u)(\nu_u-\nu)}\right] \quad , \tag{11}$$

where ν_u is the undrained Poisson's ratio, defined by

$$\nu_u = \frac{3\nu + \alpha B(1-2\nu)}{3-\alpha B(1-2\nu)} \quad . \tag{12}$$

The undrained condition denotes fluid is trapped in the porous solid, such that $\zeta = 0$.

3. Formulation and solution

3.1 Formulation of the poroelastic problem

We consider the two-dimensional poroelastic material model shown in Fig. 1, with a width $2a$ in the x-direction and a unit thickness. The sample is sandwiched between two rigid and impermeable plates at the top and bottom, and subjected to cyclic axial loading and bending moment. The edges of the model $x = \pm a$ are assumed to be stress-free and drained, i.e. the fluid pressure p satisfies:

$$p(x = \pm a, t) = 0 \quad . \tag{13}$$

This boundary condition denotes that the fluid can freely leak from the edges. Both a cyclic axial load per unit thickness $N(t)$ with amplitude N_0 and a cyclic bending moment per unit thickness $M(t)$ with amplitude M_0 are applied in the same phase along the *y*-direction at time $t = 0$ through the rigid plates. The boundary conditions for stresses are given as:

$$\int_{-a}^{a} \sigma_{yy} dx = -N(t) = -N_0 \sin \omega t \tag{14}$$

$$\int_{-a}^{a} x\sigma_{yy} dx = -M(t) = -M_0 \sin \omega t \quad , \tag{15}$$

where ω is the angular frequency of the cyclically applied load and moment. The initial condition of the poroelastic material is assumed to be at rest, that is $\sigma_{ij}(x, t=0) = 0$ and $p(x, t=0) = 0$.

Considering the problem symmetry, the stress components σ_{ij} and fluid pressure p depend only on x and t. Assuming no shear stresses throughout the poroelastic material, i.e. $\sigma_{xy}(x, t) = 0$, stress equilibrium, Eq. (6) requires $\sigma_{xx}(x, t) = 0$. Moreover, under a plane strain condition in the *z*-direction, the constitutive relations yield:

$$\sigma_{kk} = (1+\nu)\sigma_{yy} - (1-2\nu)\alpha p \quad . \tag{16}$$

Substituting Eq. (16) into Eqs. (8) and (10), the strain compatibility and diffusion equations are reduced to:

$$\frac{\partial^2}{\partial x^2}\left[\sigma_{yy} + \frac{\alpha(1-2\nu)}{(1-\nu)} p\right] = 0 \tag{17}$$

$$c\frac{\partial^2}{\partial x^2}\left[\sigma_{yy} + \frac{3}{B(1+\nu_u)} p\right] = \frac{\partial}{\partial t}\left[\sigma_{yy} + \frac{3}{B(1+\nu_u)} p\right] \quad . \tag{18}$$

Introducing the dimensionless parameters:

$$x^* \equiv \frac{x}{a}, \quad t^* \equiv \frac{ct}{a^2}$$

$$\sigma_{ij}^{*} \equiv \frac{2a\sigma_{ij}}{N_0}, \quad p^{*} \equiv \frac{p}{B\left(1+\nu_u\right) N_0 / 6a}$$

$$H \equiv \frac{1-\nu}{\nu_u - \nu}, \quad \Omega \equiv \frac{a^2 \omega}{c}, \quad \Lambda \equiv \frac{3M_0}{aN_0} \quad , \tag{19}$$

the strain compatibility equation, Eq. (17), the diffusion equation, Eq. (18) and the boundary conditions, Eqs. (13)–(15) reduce to

$$\frac{\partial^2}{\partial x^{*2}}\left(\sigma_{yy}^{*} + \frac{1}{H} p^{*} \right) = 0 \tag{20}$$

$$\frac{\partial^2}{\partial x^{*2}}\left(\sigma_{yy}^{*} + p^{*} \right) = \frac{\partial}{\partial t^{*}}\left(\sigma_{yy}^{*} + p^{*} \right) \tag{21}$$

$$p^{*}\left(x^{*} = \pm 1, \, t^{*} \right) = 0 \tag{22}$$

$$\int_{-1}^{1} \sigma_{yy}^{*} dx^{*} = -2 \sin \Omega t^{*} \tag{23}$$

$$\int_{-1}^{1} x^{*} \sigma_{yy}^{*} dx^{*} = -\frac{2}{3} \Lambda \sin \Omega t^{*} \quad . \tag{24}$$

Hereinafter, H is called the dimensionless stress coefficient, Ω is called the dimensionless frequency, and Λ is called the axial-bending loading ratio. Eventually, this poroelastic problem results in the system of the partial differential equations Eqs. (20) and (21) under the boundary conditions of Eqs. (22)–(24).

3.2 Solution of fluid pressure

We solve the boundary value problem shown in the previous section for fluid pressure p^{*}. The integration of Eq. (20) yields:

$$\sigma_{yy}^{*}\left(x^{*}, \, t^{*} \right) + \frac{1}{H} p^{*}\left(x^{*}, \, t^{*} \right) = C_1\left(t^{*} \right) x^{*} + C_2\left(t^{*} \right) \quad , \tag{25}$$

where C_1 and C_2 are proportional constants that depend only on time t^{*}. Substituting $x^{*} = \pm 1$

into Eq. (25) using the diffusion equation, Eq. (21), C_1 and C_2 are expressed in the form:

$$C_1\left(t^*\right)=\frac{1}{2}\left\{\sigma_{yy}^*\left(1,\, t^*\right)-\sigma_{yy}^*\left(-1,\, t^*\right)\right\} \tag{26}$$

$$C_2\left(t^*\right)=\frac{1}{2}\left\{\sigma_{yy}^*\left(1,\, t^*\right)+\sigma_{yy}^*\left(-1,\, t^*\right)\right\} \quad . \tag{27}$$

Substituting Eq. (25) into Eq. (21) to eliminate the fluid pressure p^* leads to the partial differential equation for the stress σ_{yy}^*:

$$\frac{\partial^2\sigma_{yy}^*\left(x^*,\, t^*\right)}{\partial x^{*2}}=\frac{\partial\sigma_{yy}^*\left(x^*,\, t^*\right)}{\partial t^*}+\frac{H}{1-H}\left\{\frac{dC_1\left(t^*\right)}{dt^*}x^*+\frac{dC_2\left(t^*\right)}{dt^*}\right\} \quad . \tag{28}$$

Taking the Laplace transform of Eq. (28) with the assumption of no stress under the initial conditions, the general solution of Eq. (28) is obtained:

$$\tilde{\sigma}_{yy}^*\left(x^*,\, s\right)=A(s)\cosh\sqrt{s}x^*+B(s)\sinh\sqrt{s}x^*-\frac{H}{1-H}\left\{\tilde{C}_1(s)\,x^*+\tilde{C}_2(s)\right\} \quad , \tag{29}$$

where the tilde (˜) signifies the Laplace transform, and $A(s)$ and $B(s)$ are unknown coefficients to be determined from the boundary conditions. Substituting $x^* = \pm 1$ into Eq. (29) and using the Laplace transform of Eqs. (26) and (27) yields:

$$\tilde{C}_1(s)=(1-H)\,B(s)\sinh\sqrt{s} \tag{30}$$

$$\tilde{C}_2(s)=(1-H)\,A(s)\cosh\sqrt{s} \quad . \tag{31}$$

Therefore, substitution of Eqs. (30) and (31) into Eq. (29) leads to

$$\begin{aligned}\tilde{\sigma}_{yy}^*\left(x^*,\, s\right)=A(s)\left\{\cosh\sqrt{s}x^*-H\cosh\sqrt{s}\right\}+\\ B(s)\left\{\sinh\sqrt{s}x^*-x^*H\sinh\sqrt{s}\right\}\end{aligned} \quad . \tag{32}$$

Application of the Laplace transforms of the boundary conditions Eqs. (23) and (24), and the use of Eq. (32) yield:

$$A(s)=-\frac{\dfrac{\Omega}{s^2+\Omega^2}\sqrt{s}}{\sinh\sqrt{s}-H\sqrt{s}\cosh\sqrt{s}} \tag{33}$$

$$B(s) = -\frac{\Lambda \dfrac{\Omega}{s^2 + \Omega^2} s}{3\sqrt{s}\cosh\sqrt{s} - \sinh\sqrt{s}\left(3 + Hs\right)}. \tag{34}$$

Thus, all the unknown parameters are determined.

By substituting Eqs. (30)–(32) into the Laplace transform of Eq. (25), the Laplace transform of the fluid pressure $p^*\left(x^*, t^*\right)$ is expressed as:

$$\begin{aligned}\tilde{p}^*\left(x^*, s\right) = A(s) H\left\{\cosh\sqrt{s} - \cosh\sqrt{s}x^*\right\} + \\ B(s) H\left\{x^* \sinh\sqrt{s} - \sinh\sqrt{s}x^*\right\}\end{aligned} . \tag{35}$$

By applying the inverse Laplace transform of Eq. (35) with the help of Eqs. (33) and (34), the fluid pressure $p^*\left(x^*, t^*\right)$ can eventually be derived as the sum of the transient response $p^*_{trans}\left(x^*, t^*\right)$ and the steady-state response $p^*_{steady}\left(x^*, t^*\right)$ in the following form:

$$p^*\left(x^*, t^*\right) = p^*_{trans}\left(x^*, t^*\right) + p^*_{steady}\left(x^*, t^*\right) \tag{36}$$

$$\begin{aligned}p^*_{trans}\left(x^*, t^*\right) = 2\sum_{n=1}^{\infty} \frac{\Omega\lambda_n^2 \sin\lambda_n\left(\cos\lambda_n - \cos\lambda_n x^*\right)}{\left(\lambda_n^4 + \Omega^2\right)\left(\lambda_n - \sin\lambda_n\cos\lambda_n\right)} e^{-\lambda_n^2 t^*} \\ + 2\Lambda\sum_{n=1}^{\infty} \frac{\Omega\mu_n^2\left(\sin\mu_n - \mu_n\cos\mu_n\right)\left(x^*\sin\mu_n - \sin\mu_n x^*\right)}{\left(\mu_n^4 + \Omega^2\right)\left(\mu_n^2 + \mu_n\sin\mu_n\cos\mu_n - 2\sin^2\mu_n\right)} e^{-\mu_n^2 t^*}\end{aligned} \tag{37}$$

$$\begin{aligned}p^*_{steady}\left(x^*, t^*\right) = \left(1 + \Lambda x^*\right)\sin\Omega t^* - \mathrm{Im}\left[\left\{\frac{H\sqrt{i\Omega}\cosh\sqrt{i\Omega}x^* - \sinh\sqrt{i\Omega}}{H\sqrt{i\Omega}\cosh\sqrt{i\Omega} - \sinh\sqrt{i\Omega}} + \right.\right. \\ \left.\left. \Lambda\frac{i\Omega H\sinh\sqrt{i\Omega}x^* + 3x^*\left(\sinh\sqrt{i\Omega} - \sqrt{i\Omega}\cosh\sqrt{i\Omega}\right)}{i\Omega H\sinh\sqrt{i\Omega} + 3\left(\sinh\sqrt{i\Omega} - \sqrt{i\Omega}\cosh\sqrt{i\Omega}\right)}\right\} e^{i\Omega t}\right] ,\end{aligned} \tag{38}$$

where λ_n and μ_n are, respectively, the n^{th} solutions of

$$\frac{\tan\lambda_n}{\lambda_n} = H \tag{39}$$

$$\frac{\tan\mu_n}{\mu_n} = \frac{3}{3 - H\mu_n^2} \quad . \tag{40}$$

Equations (36)–(40) show that the fluid pressure $p^*\left(x^*, t^*\right)$ depends on three dimensionless parameters, H, Ω, and Λ.

4. Results

4.1 Fluid pressure behavior

As shown in Eqs. (36)–(40), the dimensionless fluid pressure $p^*\left(x^*, t^*\right)$ in a poroelastic material is expressed as a function of the normalized position x^* and time t^*, and depends on the dimensionless parameters H, Ω and Λ. The dimensionless stress coefficient H is the parameter related to the material properties of matrix material and interstitial fluid that make up the poroelastic material. Both the dimensionless frequency Ω and the axial-bending loading ratio Λ are determined by the loading conditions, representing temporal and spatial characteristics. Kameo *et al*. (2008) reported that the distribution and evolution of fluid pressure under cyclic loading are almost independent of the dimensionless stress coefficient H when H is larger than 50, because the effect of fluid-to-solid coupling becomes negligible compared to that of solid-to-fluid coupling. To investigate the dependence of fluid pressure on the loading condition, we demonstrate how the dimensionless parameters Ω and Λ affect the fluid pressure behavior in poroelastic material, with H = 100.

We investigated the effect of the dimensionless frequency Ω on the behavior of fluid pressure $p^*\left(x^*, t^*\right)$. The dimensionless parameter Ω defined in Eq. (19) represents the ratio of the characteristic time of the fluid pressure relaxation, $\tau_r = a^2/c$, to that of the applied load, $\tau_f = 1/\omega$. The fluid pressure distributions along the x-direction for Ω = 0.1, 1, 10 and

100, with Λ = 1, are shown in Fig. 2. Figure 2a corresponds to the steady-state response $p^*_{steady}\left(x^*, t^*\right)$ plotted for eight equal length phase points in a period, and Fig. 2b corresponds to the transient response $p^*_{trans}\left(x^*, t^*\right)$ plotted at t^* = 0, 0.01, 0.1 and 1. The fluid pressure evolution at x^* = 0 for Ω = 0.1, 1, 10 and 100, with Λ = 1, is shown in Fig. 3. In each set of figures, the upper one is the enlarged graph of the lower one from the initial time to the 1/12 period of the corresponding loading curve.

In addition, we investigated the effect of the axial-bending loading ratio Λ on the pressure p^*. The parameter Λ stands for the ratio of the magnitude of the bending moment to that of the axial load, referring to Eq. (19). The fluid pressure distributions for Λ = 0.1, 1, 10 and 100, with Ω = 1, are shown in Fig. 4. Figures 4a and b correspond to the steady-state response $p^*_{steady}\left(x^*, t^*\right)$ and the transient response $p^*_{trans}\left(x^*, t^*\right)$, respectively.

To quantify the transient properties of fluid pressure, we introduce two factors. One factor is the half-value period of the transient stage $T_{1/2}$, which is defined by

$$T_{1/2} \equiv \frac{\Omega}{2\pi}\left(\int_{-1}^{1}\left|P^*_{trans}\right| dx^*\right)_{1/2} \quad , \tag{41}$$

where $(\ )_{1/2}$ signifies the dimensionless time interval required for the quantity in parenthesis to decay to half of its initial value. The half-value period $T_{1/2}$ quantifies the decay-rate of the integration value of p^*_{trans} over the width normalized by the period of applied cyclic loading. The other factor is the contribution factor of the transient response Π, which is defined by

$$\Pi \equiv \frac{\int_0^{\frac{2\pi}{\Omega}}\left(\int_{-1}^{1}\left|P^*_{trans}\right| dx^*\right) dt^*}{\int_0^{\frac{2\pi}{\Omega}}\left(\int_{-1}^{1}\left|P^*_{steady}\right| dx^*\right) dt^*} \quad . \tag{42}$$

Considering that the fluid pressure $p^*\left(x^*, t^*\right)$ is expressed as the sum of the transient

response $p^*_{trans}\left(x^*, t^*\right)$ and the steady-state response $p^*_{steady}\left(x^*, t^*\right)$ as shown in Eq. (36), Π represents the ratio of the magnitude of the transient response to that of the steady-state response in the first period of the loading cycle. Both the half-value period of the transient stage $T_{1/2}$ and the contribution factor of the transient response Π are functions of the dimensionless frequency Ω and the axial-bending loading ratio Λ when the dimensionless stress coefficient H is constant. To investigate the effects of Ω and Λ on these two factors, Figs. 5 and 6 show $T_{1/2}$ and Π three-dimensionally plotted versus $\log_{10}\Lambda$ and $\log_{10}\Omega$, respectively.

4.2 Steady-state response

The steady-state solution of fluid pressure in a three-dimensional poroelastic beam subjected to cyclic loading has already presented by Zhang and Cowin (1994). Assuming the plane strain condition and free leakage at surfaces in their problem, their analysis conditions reduce to those of our work. Figure 2a, which shows the behavior of fluid pressure distribution as the dimensionless frequency Ω changes, and Fig. 4a, which shows the behavior of fluid pressure distribution as the axial-bending loading ratio Λ changes, corresponds to the solution obtained in their work. In this section, we summarize the fluid pressure behavior in steady state obtained by our study and previous studies, and focus on the seepage velocity of interstitial fluid flow.

Figure 2a shows that, as the dimensionless frequency Ω increases, the fluid pressure p^*_{steady} also increases, because the excess fluid pressure has difficulty diffusing due to the rapid

change in applied loading. The fluid pressure profile along the x-direction transforms from a parabolic to a linear shape. Following Darcy's law, which describes a proportional relationship between a fluid flux and a fluid pressure gradient, the seepage velocity of the interstitial fluid becomes higher near the surface in the positive region of x-coordinates, as the dimensionless frequency Ω increases. Meanwhile, Fig. 3 (i) indicates that there is a remarkable phase shift between the applied cyclic loading and the corresponding fluid pressure evolution in a steady state at $x^* = 0$ at low frequency $\Omega = 0.1$ due to the interstitial fluid transport. At high frequency, when Ω is larger than 10, the profiles are almost in phase because the interstitial fluid has difficulty moving, as shown in Figs. 3 (iii) and (iv).

The dimensionless parameter Λ represents the ratio of the magnitude of the bending moment to that of the axial load, as mentioned in the previous section. Recalling that the fluid pressure p is normalized by the amplitude of axial load N_0, as shown in Eq. (19), we can consider the axial-bending loading ratio Λ as the dimensionless bending moment when N_0 is constant. Figure 4a indicates that the fluid pressure p^*_{steady} increases with Λ due to the additional bending moment. As shown in Fig. 4a (i), the fluid pressure profile has a symmetric shape about $x^* = 0$ when the magnitude of axial load is much larger than that of the bending moment, $\Lambda = 0.1$. The increase of Λ causes a sign inversion of the fluid pressure around both surfaces of the poroelastic material, as shown in Fig. 4a (iii), and when the bending moment is dominant, compared to the axial load, $\Lambda = 100$, the fluid pressure profile has an antisymmetric shape about $x^* = 0$, as shown in Fig. 4a (iv). This transition of the fluid pressure profile with an increasing axial-bending loading ratio Λ induces interstitial fluid flow,

not only in the neighborhood of the material surfaces, but also around the center of the material far from the surfaces.

4.3 Transient response

The transient stage of fluid pressure lasts for some time after applying cyclic loading to the poroelastic material until the fluid pressure reaches a steady state. Figures 3 (i) and (iv) indicate that the effect of the transient response is dominant when the phase shift between the fluid pressure evolution in the steady state and the applied cyclic loading is remarkable. Considering that the sum of the transient response p^*_{trans} and the steady-state response p^*_{steady} at the initial time $t^* = 0$ must be null because the applied loading is null at this time, the transient response is related to such a phase shift, and compensates for it immediately after the application of loading. As a result, an increase in the rate of change in fluid pressure is observed in the transient stage, as indicated clearly in Figs. 3 (i) and (ii).

As mentioned in the previous section, the fluid pressure evolution and the applied cyclic loading are almost in phase for a large dimensionless frequency Ω because the fluid pressure has difficulty diffusing. As shown in Figs. 2a (iii) and (iv), for fluid pressure distributions in steady state, both the applied loading and the fluid pressure change in the same phase around the negative region of the x-coordinates, where the pressure profile has a linear shape. This suggests that the effect of the transient response is limited to the region close to the surfaces of the poroelastic material when Ω is large, as shown in Fig. 2b. Meanwhile, Fig. 4b indicates that the fluid pressure profile in transient state transforms from a symmetric shape about $x^* =$

0 to an antisymmetric shape about $x^* = 0$ as the axial-bending loading ratio Λ increases, similar to the pressure profile in steady state.

Figure 5 is a three-dimensional plot of the half-value period $T_{1/2}$ representing the decay rate of the transient stage as the axial-bending loading ratio Λ and the dimensionless frequency Ω change. This figure shows that $T_{1/2}$ reaches a plateau at 0.29, as Ω increases. In addition, $T_{1/2}$ has a peak value, 0.36, when Λ is smaller than 1 ($\log_{10}\Lambda < 0$) and Ω is about 10 ($\log_{10}\Omega \sim 1$). These results reveal that the effect of the transient response is reduced by half in the first 0.4 period of the applied cyclic loading.

Figure 6 shows the behavior of the contribution factor of the transient response Π as a function of Λ and Ω. There is a spike of Π around $\Omega = 10$ ($\log_{10}\Omega = 1$) with a peak value of 0.20, while the value of Ω that maximizes Π depends on whether Λ is larger than 1 ($\log_{10}\Lambda > 0$). This suggests that the magnitude of the transient response is about 20% that of the steady-state response under certain conditions. Unlike the behavior of $T_{1/2}$, Π gradually declines after the peak with increasing Ω because, under a large dimensionless frequency Ω, the effect of the transient response becomes negligible in the region, except for the neighborhood of the material surfaces, as shown in Fig. 2b (iv).

5. Discussion

We presented an analytical solution for interstitial fluid pressure in poroelastic materials subjected to cyclic axial and bending loading. The analytical solution contains steady-state and transient responses—both depend on three dimensionless parameters: The dimensionless

stress coefficient H governing solid-fluid coupling behavior in poroelastic materials, the dimensionless frequency Ω that stands for the ratio of the characteristic time of the fluid pressure relaxation to that of applied load, and the axial-bending loading ratio Λ that represents the ratio of the magnitude of the bending moment to that of the axial load. In this study, we focused on poroelastic materials that have a sufficiently large value of H to neglect the effect of fluid-to-solid coupling, and investigated the behavior of interstitial fluid pressure with the change of two dimensionless parameters Ω and Λ.

There are many reports on the mechanical behavior of poroelastic materials under cyclic loading in a variety of fields, such as geomechanics (e.g. Jacob, 1940; Bredehoeft, 1967; Rojstaczer, 1988; Quilty and Roeloffs, 1991; Roeloffs, 1996) and biomechanics (e.g. Harrigan and Hamilton, 1993; Weinbaum *et al*., 1994; Zhang and Cowin, 1994, Zhang *et al*., 1997; Swan *et al*., 2003). Even though understanding poroelastic behavior in detail requires investigating the transient response observed immediately after loading, few reports have addressed the phenomenon. The importance of the transient stage has only been recognized using finite element analysis (Manfredini *et al*., 1999). Kameo *et al*. (2008) obtained the first analytical solution of fluid pressure including the transient response in poroelastic materials under cyclic uniaxial loading. In this study, we extended the solution by considering bending moment as well as uniaxial load. This generalization made it possible to theoretically analyze the both transient and steady-state responses of poroelastic materials under more complex cyclic loading conditions.

The transient stage prior to the steady state was confirmed using a finite element analysis of

a three-dimensional poroelastic beam under cyclic loading (Manfredini *et al*., 1999). In their study, it was reported that the duration of the transient stage was confined almost in the first cycle of the loading curve. In the case of free leakage at the surface of the poroelastic material, which corresponds to our boundary condition, they showed the following characteristics of the fluid pressure evolution around the center far from the surfaces. (i) When the dimensionless frequency is low ($\Omega = 0.1$), there is an immediately sharp increase in the rate of change of fluid pressure in the transient stage, and it leads 1/4 phase shift between the fluid pressure evolution and the applied cyclic loading in the steady state. (ii) When the dimensionless frequency is high ($\Omega = 100$), the influence of the transient response is almost negligible, and the fluid pressure evolution and the applied cyclic loading are in phase in the steady state. All the above fluid pressure behaviors reported by Manfredini *et al*. (1999) agree with our results (see Fig. 3). This suggests the validity of the analytical solution we obtained in this study.

To evaluate the transient properties of fluid pressure quantitatively, we introduced two factors: The half-value period $T_{1/2}$, defined by Eq. (41), and the contribution factor Π, defined by Eq. (42). As shown in Figs. 5 and 6, the behavior of both factors with an increase in the dimensionless frequency Ω depends on whether Λ is larger than 1. This is because the stress distribution for the case $\Lambda > 1$ has specific characteristics—i.e. there is a region where the stress σ_{yy} is neutral in the poroelastic material. Thus, whether the value of Λ is larger than 1 is key to the poroelastic analysis of transient response. Except for such Λ-dependence, $T_{1/2}$ and Π depend almost only on the dimensionless frequency Ω and have peak values around Ω

= 10. This suggests that the transient response has a comparable magnitude to the steady-state response and can significantly affect the mechanical behavior of poroelastic materials when Ω is about 10.

As far as the applied cyclic loading can be regarded as quasi-static, the interstitial fluid pressure behavior described in this study is commonly observed in various poroelastic materials, such as living bone. The mechanical behavior of living bone, which contains a bone matrix (solid phase) and interstitial fluid (fluid phase), can be modeled as a poroelastic material (Cowin, 1999). For a physiological range of activities excluding shocks, living bone experiences only low frequencies of loading (Rémond and Naili, 2005, Rémond *et al*., 2008) and shows the quasi-static mechanical behavior. Many researchers have suggested that poroelasticity is an appropriate theory for investigating the coupled diffusion-deformation mechanisms in bone (e.g. Nowinski and Davis, 1970; Johnson *et al*., 1982; Johnson, 1984; Kufahl and Saha, 1990; Williams, 1992). In this section, we focus on trabecular bone, the microstructural elements of cancellous bone. The trabeculae within the human body are usually subjected to low-frequency cyclic loading due to locomotion (1–2 Hz) and maintenance of posture (15–20 Hz) (Weinbaum *et al*., 1994). Mechanical loading induces an interstitial fluid flow in a lacuno-canalicular system, which has small pores and vessels with a diameter on the order of 100 nm (You *et al*., 2004). The interstitial fluid flow is believed to play an important role not only in providing nutrients and removing wastes but also in the cellular mechanotransduction (Wang *et al*., 2007), and that can lead to the regulation of trabecular bone remodeling (Burger and Klein-Nulend, 1999). Therefore, trabecular

architecture formed by bone remodeling in cancellous bone is closely related to the mechanical environment (Wolff, 1869, 1892, 1986); its regulation process at a microscopic cellular level has been investigated in detail in the context of bone functional adaptation by remodeling, through modeling and simulation studies (Adachi *et al*., 2001; Tsubota *et al*., 2002; Ruimerman *et al*., 2005).

Two factors influence the mechanical behavior of trabeculae—the material properties and the loading conditions. In the case of two dimensional poroelastic materials subjected to cyclic loading, the former is represented by the dimensionless stress coefficient H and the latter by the dimensionless frequency Ω and the axial-bending loading ratio Λ. By using the reported material parameters of trabeculae (Cowin, 1999, Smit *et al*., 2002), the dimensionless stress coefficient H is derived as 80–100. This indicates that the H of trabeculae is sufficiently large that the interstitial fluid behavior is nearly independent of H. Meanwhile, the dimensionless frequency Ω depends not only on the angular loading frequency ω but also on the model size and material properties represented by a and c, referring to Eq. (19). The value of Ω increases as the characteristic length of the model a increases or the diffusion coefficient c decreases, i.e. the permeability k decreases, even though ω is constant. Thus, the quasi-static assumption in this study does not impose a limit on the value of dimensionless frequency Ω unless a and c are fixed. Considering the material parameters of trabeculae and bone permeability at the microscopic lacuno-canalicular level, $k = 10^{-22}$–10^{-19} m^2, (Beno *et al*., 2006) with the assumption of the physiological loading frequency ranging from 1 to 20 Hz, the dimensionless frequency Ω trabeculae experience in

daily activities is estimated at 10^{-2}–10^{2}. The dimensionless frequency Ω varies over such a wide range of values because the permeability k in Eq. (11) is very difficult to determine, leading to an estimation ranging over several orders of magnitude. The estimated order of the magnitude of Ω covers the range of dimensionless frequencies where the contribution of transient response is comparatively large ($\Omega \sim 10$). This suggests that consideration of the effect of transient response is critical for the analysis of interstitial fluid flow in trabeculae. The axial-bending loading ratio Λ depends on the trabecular region, and is expected to have a wide range of values from zero to infinity. It seems reasonable to assume that the variation of Ω and Λ in trabeculae induces the variety of mechanical stimuli that osteocytes sense via interstitial fluid flow, and as a result, bone formation and resorption are appropriately regulated.

A theoretical approach to the poroelastic problems is extremely useful for comprehending the essence of the mechanical behavior of poroelastic materials. However, it is generally difficult to derive a closed form solution of given initial/boundary value problems, except for the cases involving simple geometries and loading conditions. To solve poroelastic problems with more complex geometry and boundary conditions, a numerical simulation based on a finite element method or a boundary element method can be a powerful tool. Poroelastic analysis will make significant contributions to our understanding of the crucial phenomena associated with solid-fluid coupling behavior in various research fields through the complementary usage of both the theoretical and numerical approaches.

Acknowledgement

This work was partly supported by the Grant-in-Aid for Scientific Research from the Ministry of Education, Culture, Sports, Science and Technology of Japan.

References

Adachi, T., Tsubota, K., Tomita, Y., Hollister, S.J., 2001. Trabecular surface remodeling simulation for cancellous bone using microstructural voxel finite element models. J. Biomech. Eng. 123 (5), 403-409.

Beno, T., Yoon, Y.J., Cowin, S.C., Fritton, S.P., 2006. Estimation of bone permeability using accurate microstructural measurements. J. Biomech. 39 (13), 2378-2387.

Biot, M.A., 1941. General theory of three-dimensional consolidation. J. Appl. Phys. 12 (2), 155-164.

Biot, M.A., 1955. Theory of elasticity and consolidation for a porous anisotropic solid. J. Appl. Phys. 26 (2), 182-185.

Bredehoeft, J.D., 1967. Response of well-aquifer systems to earth tides. J. Geophys. Res. 72 (12), 3075-3087.

Burger, E.H., Klein-Nulend, J., 1999. Mechanotransduction in bone - role of the lacuno-canalicular network. FASEB J. 13, S101-S112.

Coussy, O., 2004. Poro Mechanics. John Wiley & Sons, Ltd, England, 298p.

Cowin, S.C., 1999. Bone poroelasticity. J. Biomech. 32 (3), 217-238.

Detournay, E., Cheng, A.H.-D., 1993. Fundamentals of poroelasticity. Chapter 5 in Comprehensive Rock Engineering: Principles, Practice and Projects, Vol. II, Analysis and Design Method, ed. C. Fairhurst, Pergamon Press, 113-171.

Harrigan, T.P., Hamilton, J.J., 1993. Bone strain sensation via transmembrane potential changes in surface osteoblasts: loading rate and microstructural implications. J. Biomech. 26 (2), 183-200.

Jacob, C.E., 1940. On the flow of water in an elastic artesian aquifer. Trans. Am. Geophys. Union 22, 783-787.

Johnson, M.W., Chakkalakal, D.A., Harper, R.A., Katz, J.L., Rouhana, S.W., 1982. Fluid flow in bone in vitro. J. Biomech. 15 (11), 881-885.

Johnson, M.W., 1984. Behavior of fluid in stressed bone and cellular-stimulation. Calcif. Tissue Int. 36 (Suppl. 1), S72-S76.

Kameo, Y., Adachi, T., Hojo, M., 2008. Transient response of fluid pressure in a poroelastic material under uniaxial cyclic loading. J. Mech. Phys. Solids 56 (5), 1794-1805.

Kufahl, R.H., Saha, S., 1990. A theoretical model for stress-generated fluid flow in the canaliculi-lacunae network in bone tissue. J. Biomech. 23 (2), 171-180.

Manfredini, P., Cocchetti, G., Maier, G., Redaelli, A., Montevecchi, F.M., 1999. Poroelastic finite element analysis of a bone specimen under cyclic loading. J. Biomech. 32 (2),

135-144.
Mow, V.C., Kuei, S.C., Lai, W.M., Armstrong, C.G., 1980. Biphasic creep and stress-relaxation of articular-cartilage in compression: thory and experiments. J. Biomech. Engng 102 (1), 73-84.
Nowinski, J.L., Davis, C.F., 1970. A model of the human skull as a poroelastic spherical shell subjected to a quasistatic load. Math. Biosci. 8, 397-416.
Quilty, E.G., Roeloffs, E.A., 1991. Removal of barometric pressure response from water level data. J. Geophys. Res. 96 (B6), 10209-10218.
Rémond, A., Naili, S., 2005. Transverse isotropic poroelastic osteon model under cyclic loading. Mech. Res. Comm. 32(6), 645-651.
Rémond, A., Naili, S., Lemaire, T., 2008. Interstitial fluid flow in the osteon with spatial gradients of mechanical properties: a finite element study. Biomech. Model. Mechanobiol. 7, 487-495.
Roeloffs, E.A., 1996. Poroelastic techniques in the study of earthquake-related hydrologic phenomena. Adv. Geophys. Academic Press Inc, San Diego, pp. 135-195.
Rojstaczer, S., 1988. Determination of fluid-flow properties from the response of water levels in wells to atmospheric loading. Water Resour. Res. 24 (11), 1927-1938.
Ruimerman, R., Hilbers, P., van Rietbergen, B., Huiskes, R., 2005. A theoretical framework for strain-related trabecular bone maintenance and adaptation. J. Biomech. 38 (4), 931-941.
Smit, T.H., Huyghe, J.M., Cowin, S.C., 2002. Estimation of the poroelastic parameters of cortical bone. J. Biomech. 35 (6), 829-835.
Swan, C.C., Lakes, R.S., Brand, R.A., Stewart, K.J., 2003.Micromechanically based poroelastic modeling of fluid flow in haversian bone. J. Biomech. Eng. 125 (1), 25-37.
Tsubota, K., Adachi, T., Tomita, Y., 2002. Functional adaptation of cancellous bone in human proximal femur predicted by trabecular surface remodeling simulation toward uniform stress state. J. Biomech. 35 (12), 1541-1551.
Wang, H.F., 2000. Theory of Linear Poroelasticity with Applications to Geomechanics and Hydrogeology. Princeton Univ. Press, Princeton, 287p.
Wang, Y.L., McNamara, L.M., Schaffler, M.B., Weinbaum, S., 2007. A model for the role of integrins in flow induced mechanotransduction in osteocytes. Proc. Natl. Acad. Sci. USA 104 (40), 15941-15946.
Weinbaum, S., Cowin, S.C., Zeng, Y., 1994. A model for the excitation of osteocytes by mechanical loading-induced bone fluid shear stresses. J. Biomech. 27 (3), 339-360.
Williams, J.L. 1992. Ultrasonic wave propagation in cancellous and cortical bone: prediction of some experimental results by Biot's theory. J. Acoust. Soc. Am. 91 (2), 1106-1112.
Wolff, J., 1869. Ueber die bedeutung der architectur der spongiosen substanz fur die frange vom knochenwachsthum. Zentralblatt fur die medizinischen wissenschaften 6, 223-234.
Wolff, J., 1892. Das gesetz der transformation der knochen. Hirschwald, Berlin.
Wolff, J., 1986. The law of bone remodeling. (Trans. P. Maquet and R. Furlong), Springer.
Yang, M., Taber, L.A., 1991. The possible role of poroelasticity in the apparent viscoelastic behavior of passive cardiac muscle. J. Biomech. 24 (7), 587-597.

You, L., Weinbaum, S., Cowin S.,C., Schaffler M.B., 2004. Ultrastructure of the osteocyte process and its pericellular matrix. Anat. Rec. 278-A, 505-513.

Zhang, D., Cowin, S.C., 1994. Oscillatory bending of a poroelastic beam. J. Mech. Phys. Solids 42 (10), 1575-1599.

Zhang, D., Weinbaum, S., Cowin, S.C., 1998. On the calculation of bone pore water pressure due to mechanical loading. J. Solids Struct. 35 (34-35), 4981-4997.

Figure Captions

Fig. 1. A model of a two-dimensional poroelastic material subjected to cyclic axial and bending loading.

Fig. 2. Fluid pressure distribution along the x-direction for $\Lambda = 1$. (a) Steady state response and (b) transient response.

Fig. 3. Fluid pressure evolution at $x^* = 0$ for $\Lambda = 1$. In each set of figures, the upper one is the enlarged graph of the lower one from the initial time to the 1/12 period of the corresponding loading curve.

Fig. 4. Fluid pressure distribution along the x-direction for $\Omega = 1$. (a) Steady state response and (b) transient response.

Fig. 5. The behavior of the half-value period of the transient stage $T_{1/2}$ with changes of Λ and Ω three-dimensionally plotted versus $\log_{10}\Lambda$ and $\log_{10}\Omega$.

Fig. 6. The behavior of the contribution factor of the transient response Π with changes of Λ and Ω three-dimensionally plotted versus $\log_{10}\Lambda$ and $\log_{10}\Omega$.

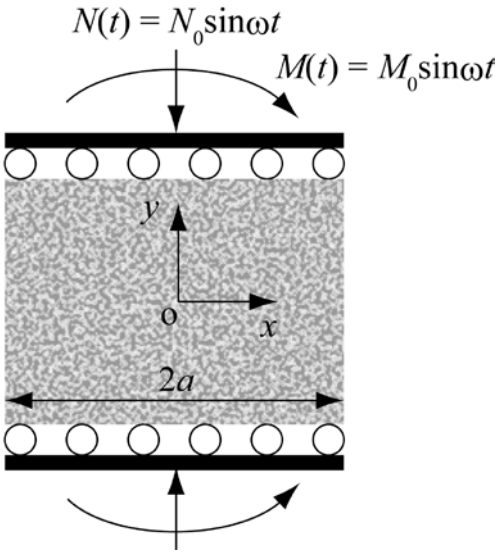

Fig. 1. A model of a two-dimensional poroelastic material subjected to cyclic axial and bending loading.

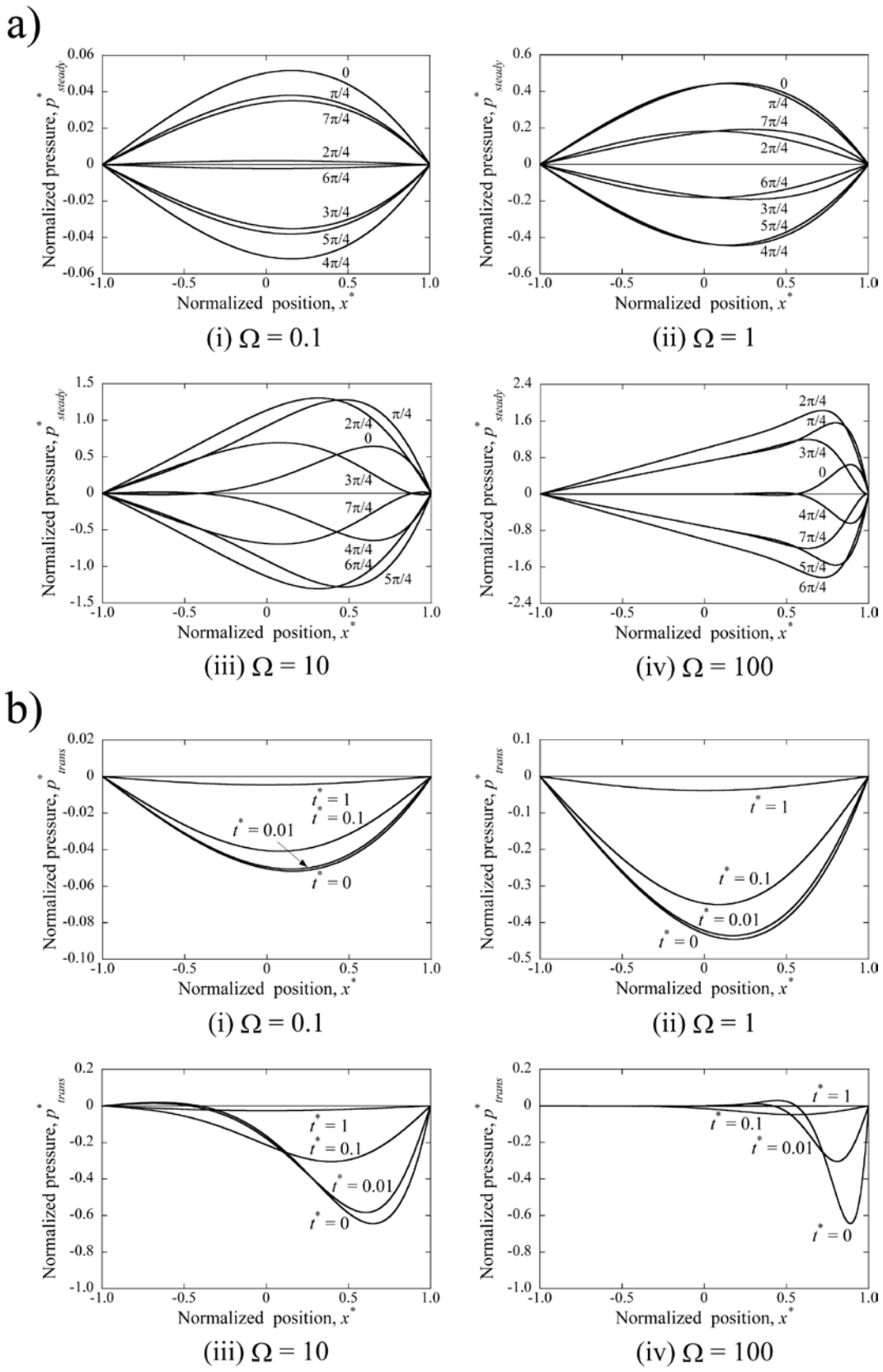

Fig. 2. Fluid pressure distribution along the x-direction for $\Lambda = 1$.
(a) Steady state response and (b) transient response.

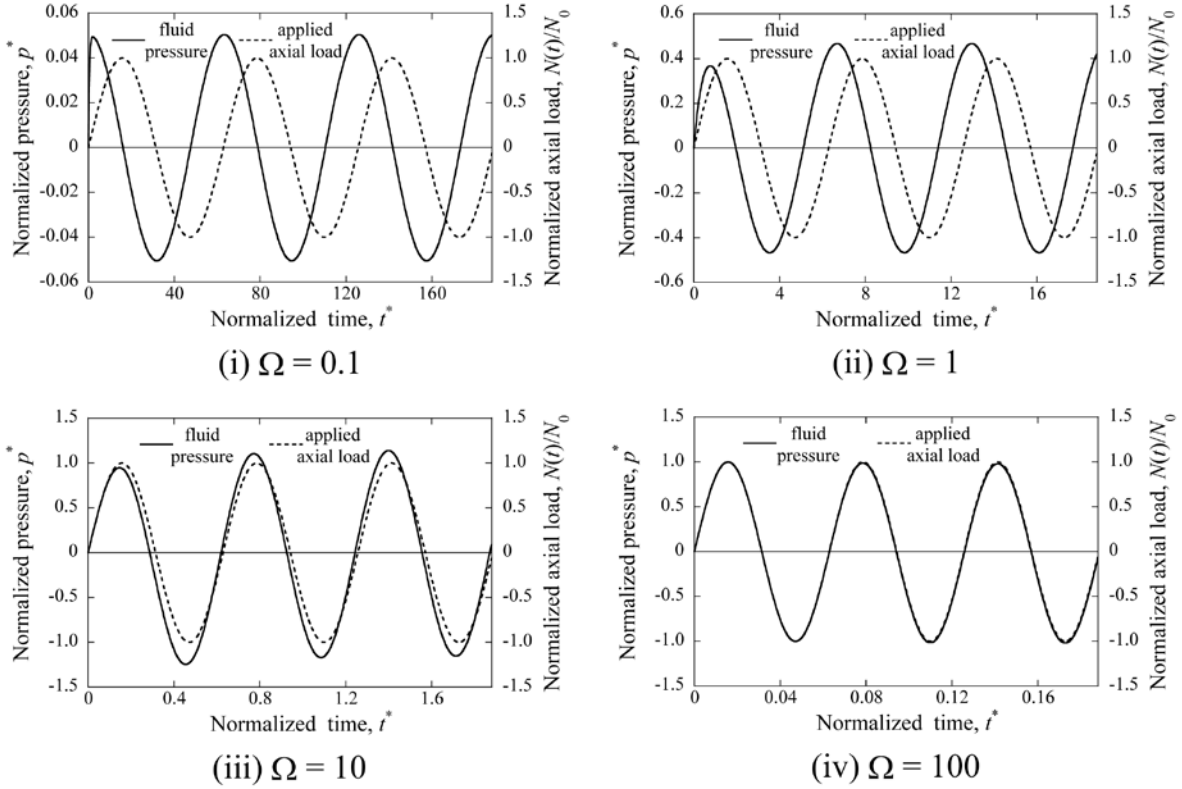

Fig. 3. Fluid pressure evolution at $x^* = 0$ for $\Lambda = 1$.

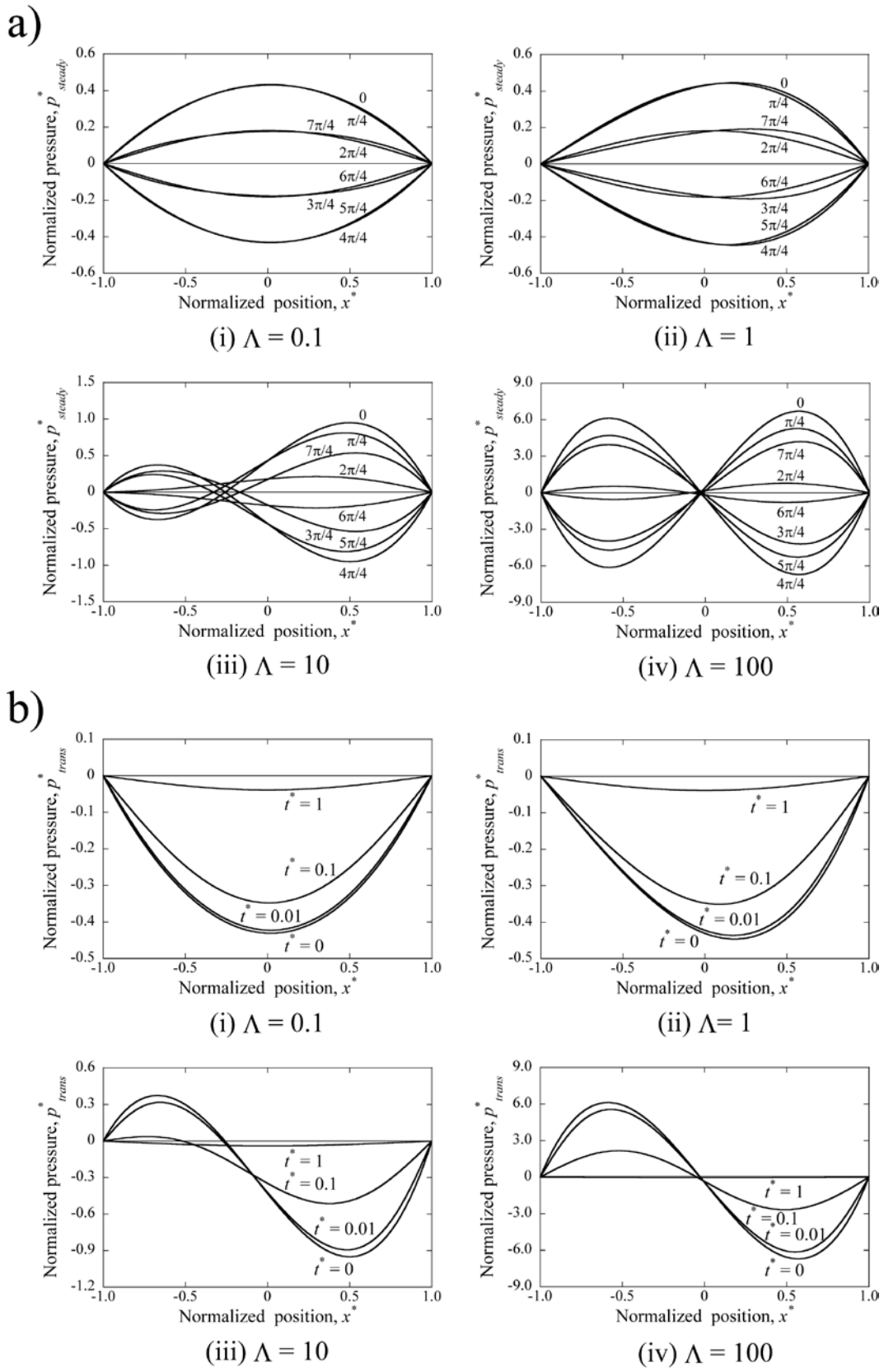

Fig. 4. Fluid pressure distribution along the x-direction for $\Omega = 1$.
(a) Steady state response and (b) transient response.

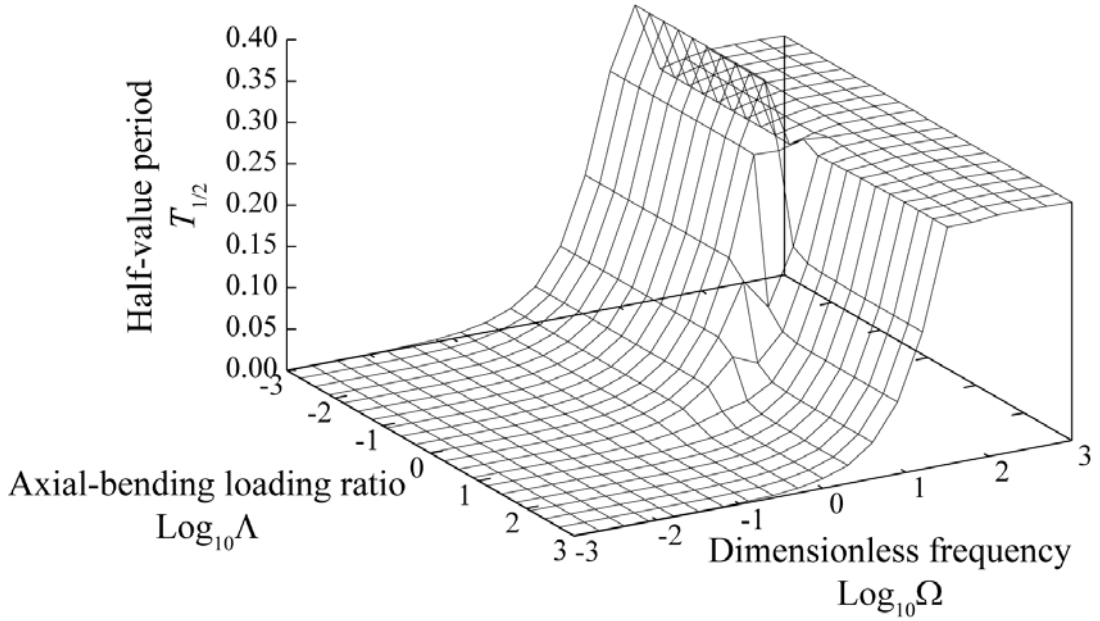

Fig. 5. The behavior of the half-value period of the transient stage $T_{1/2}$ with changes of Λ and Ω three-dimensionally plotted versus $\log_{10}\Lambda$ and $\log_{10}\Omega$.

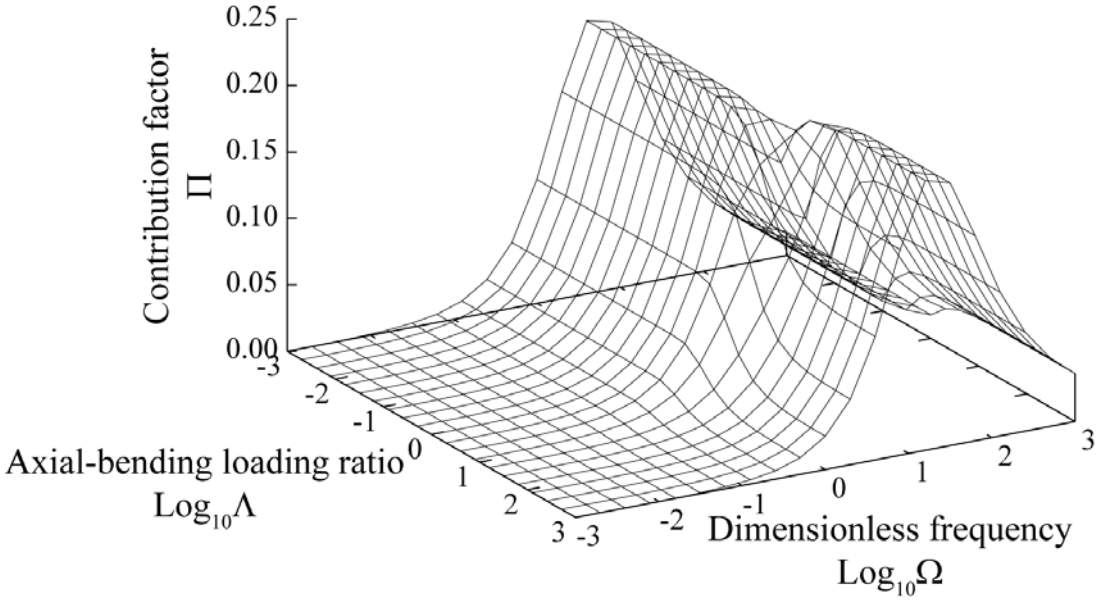

Fig. 6. The behavior of the contribution factor of the transient response Π with changes of Λ and Ω three-dimensionally plotted versus $\log_{10}\Lambda$ and $\log_{10}\Omega$.